Title

Steady state and time resolved optical characterization studies of Zn2SnO4 nanowires for solar cell applications

Journal

Journal of Applied Physics, 120(16)

ISSN

0021-8979

Authors

Yakami, Baichhabi R
Poudyal, Uma
Nandyala, Shashank R
et al.

Publication Date

2016-10-28

DOI

10.1063/1.4965697

Peer reviewed

Steady State and Time Resolved Optical Characterization Studies of Zn_2SnO_4 Nanowires for Solar Cell Applications

Baichhabi R. Yakami[1], Uma Poudyal[2], Shashank R Nandyala[1], Gaurab Rimal[2], Jason K. Cooper[3], Xuejie Zhang[4], Jing Wang[4], Wenyong Wang[2],and Jon M. Pikal[1]*

[1]*Department of Electrical and Computer Engineering, University of Wyoming, Laramie, WY 82071, USA*

[2]*Department of Physics and Astronomy, University of Wyoming, Laramie, WY 82071, USA*

[3]*Materials Science Division, Lawrence Berkeley National Laboratory, Berkeley CA 94720, USA*

[4]*Ministry of Education Key Laboratory of Bioinorganic and Synthetic Chemistry, State Key Laboratory of Optoelectronic Materials and Technologies, School of Chemistry and Chemical Engineering, Sun Yat-sen University, Guangzhou 510275, China*

[*]Contact: jpikal@uwyo.edu

ABSTRACT:

Nanowires are a promising option for sensitized solar cells, sensors, and display technology. Most of the work thus far has focused on binary oxides for these nanowires, but ternary oxides have advantages in additional control of optical and electronic properties. Here we report on the diffuse reflectance, Low Temperature (LT) and Room Temperature (RT) Photoluminescence (PL), PL Excitation (PLE) spectrum, and Time Resolved PL (TRPL) of Zinc Tin Oxide (ZTO) nanowires grown by Chemical Vapor Deposition. The PL from the ZTO nanowires does not exhibit any band gap or near gap emission, and diffuse reflectance measurement confirms that these ZTO nanowires have a direct forbidden transition. The broad PL spectrum reveals two Gaussian peaks centered at 1.86 eV (red) and 2.81 eV (blue), representing two distinct defect states or complexes. The PL spectra was further studied by Time Resolved Emission Spectrum (TRES) and intensity dependent PL and TRPL. The time resolved measurements show complex non-exponential decays at all wavelengths, indicative of defect to defect transitions, and the red emissive states decay much slower than the blue emissive states. The effects of annealing in air and vacuum are studied to investigate the origin of the defect states in the nanowires showing that the blue

states are related to oxygen vacancies. We propose an energy band model for the nanowires containing defect states within the band gap and the associated transitions between these states that are consistent with our measurements.

I. INTRODUCTION

A Gratzel Cell is a photoelectrochemical device designed to harness the energy of the sun[1], and which forms the basis of most modern sensitized solar cells. In these cells a light absorbing material (the sensitizer), which is either a dye (DSSC)[1,2] or quantum dots (QDSSC)[3,4], is attached to a high surface area material, typically a nanoparticle or nanowire film grown on a conducting substrate. These materials are enclosed by a top transparent conducting contact and the space between the two contacts is filled with an electrolyte which completes the electrical circuit. When light hits the device, the sensitizing material absorbs the energy thereby exciting electrons which are then transferred to the nanoparticle or nanowire film for transport to the back contact. The electrons which leave the sensitizing material are regenerated by the electrolyte which then transports the charge to the cathode[1].

The backbone of this system is the nanoparticle/nanowire film which is responsible for providing high density attachment of the sensitizer, fast charge separation at the interface, and efficient transport of the electrons to the anode contact[5]. While a nanoparticle film presents a very large surface area for attachment of sensitizer, the transport through the film to the anode is inhibited because electrons must hop from particle to particle, increasing the transport time and also increasing the probability that electrons will be lost along the way due to trapping and recombination[6]. Transport along nanowires is a much more efficient process due to the continuous density of states along the wire in real space[5]. In addition, nanowires have a lower surface to volume ratio, reducing the number of traps and surface recombination centers compared to nanoparticles of similar dimensions. Thus sensitized solar cells using nanowires instead of nanoparticles can have improved charge transport and collection of charge carriers[5].

To date the most widely studied materials were binary metal oxides such as TiO_2, ZnO, In_2O_3, and SnO_2. Ternary metal oxides (Zn_2SnO_4, Zn_2TiO_4, $SrTiO_3$, $CdSnO_4$, etc.) provide a broader material spectrum and thus additional control over the electrical and optical properties[2,7]. Previous reports on DSSC and QDSSC have shown that the energy band alignment between the sensitizer and the metal oxide is important for optimizing solar cell performance[8–10]. Furthermore, a direct comparative study between ZTO and TiO_2 by Villareal et al.[8] and Alvies et al.[9] suggest that ZTO provides a more optimized energy band alignment, which leads to a higher open circuit potential. As such, one path toward improving the solar energy conversion efficiency of these sensitized cells is to investigate ternary metal oxides for this purpose.

Zn_2SnO_4 (Zinc Tin Oxide, ZTO), with an inverse spinel structure, is a wide band gap (3.7 eV)[9], n-type metal oxide semiconductor[11], which is also chemically and thermodynamically stable[11,12,13]. Additionally, the high electron mobility (14 $cm^2 V^{-1} s^{-1}$)[11,14,15] of ZTO is advantageous for a transport layer in sensitized solar cells. Thus the potential application of ZTO nanowires for use as a transparent conducting oxide (anode electrode) in sensitized solar cells [7,13,10] motivates the investigation of its optical and electronic properties. The primary goal of this work is to expand our understanding of ZTO nanowires through analysis of their steady state and time resolved emission spectra, and to use this data to develop a model describing the charge carrier dynamics in these nanowires[16].

II. EXPERIMENT

The growth of ZTO nanowires was based on vapor-liquid-solid (VLS) mechanism and was reported previously[7]. A 3 nm gold layer thermally grown on silicon substrates was used as catalyst for the VLS growth. The silicon substrate was loaded at the center of a 1 inch tube furnace. The source material (0.6 g Zn foil and 0.4 g SnO powder) was positioned 5 cm upstream from the Si substrate in the

tube furnace. The tube furnace was purged by a rotary pump and nitrogen flow three times to evacuate oxygen residual before the growth. The growth temperature was 900 ^{o}C and the pressure of the tube furnace was kept at 10 torr throughout the entire growth process. A 100 sccm nitrogen flow and a 3 sccm oxygen flow were used as carrying and reactive gas, respectively. The growth temperature was held for 2 hours after which the furnace was allowed to cool down naturally. The nanowires were then etched in diluted HCL to remove any remaining ZnO, and a printing transfer process was used to move the nanowires onto a fused silica substrate as described in previous work[7]. Figure 1 a) shows a Scanning Electron Microscope (SEM) image of the nanowires which have diameters ranging from about 80 nm to 150 nm and are several tens of microns long[7]. Figure 1 b) is a typical SEM image showing the rhombohedral structured nanowire similar to what other groups have reported[17,18]. In previous work on these nanowires, HRTEM indicated the nanowires were single crystal, and the growth direction was identified as $[1\bar{1}1]$ by selected area electron diffraction (SAED)[7,10]. A more detailed description of synthesis, etching process and structural characterization of the ZTO nanowires is published elsewhere[7,10]. Characterization was conducted on the as-grown ZTO nanowires as well as samples that were annealed in air at 500° C for 12 hrs, and under vacuum at 700° C for 4 hrs.

X-Ray diffraction (XRD) was done with a Rigaku Smartlab equipped with a Cu-K_{α} source. The Raman spectrum was measured on a SnRI (IM-52). The UV-visible diffuse reflectance spectra were measured with a Perkin-Elmer Lamda 950 spectrophotometer with 150 mm integrating sphere and a Spectralon reflectance standard in the reference port. The PL excitation (PLE) spectrum was measured using Edinburgh Instruments FLS920 with 450W Xe lamp. The steady state PL spectra of the ZTO nanowires were measured using a tunable ultrafast laser as the excitation source. The ultrafast laser consisted of a regenerative Ti:Sa amplifier system that generates 4 mJ pulses at 800 nm with 100 fs pulse width and a repetition rate of 1 KHz. A portion of the 800 nm is sent to an optical parametric amplifier

(OPA) to generate a 310nm, 100 fs laser pulse which was passed through a bandpass pump clean up filter, and then focused onto the sample using mirrors. The sample PL was collected in a back scattering orientation by a high numerical aperture 90° off axis parabolic mirror. The PL spectra were measured with an Avantes CCD spectrometer using a 325 nm long pass filter to block the pump signal from entering the spectrometer. The LT PL was measured using a closed cycle liquid He refrigerator system (Model 22 Cryodyne) with custom cold finger. The measured PL spectra were corrected using a tungsten halogen lamp as a calibration source. The transient decay studies of ZTO nanowires were conducted with the same excitation setup but using Time Correlated Single Photon Counting (TCSPC). Thus the Avantes spectrometer was replaced by the combination of a 1/2m scanning monochromator, a high speed Hamamatsu Micro-Channel Plate Photomultiplier Tube (MCP-PMT R3809U-50), and photon counting board (Becker and Hickl, model: SPC 130). The operating voltage for MCP-PMT was set at -3KV. The sync pulse was generated from a small portion of the 800 nm from the regenerative amplifier and detected using a fast photodiode. An optical fiber delay line was used to delay the sync pulse to obtain the required time window for the TCSPC experiment. The instrument response function of the TCSPC system was measured to be 80 ps, limited mainly by the temporal dispersion within the monochromator. Characterization of the complex decay observed from our ZTO nanowires was accomplished by splitting the measurement into two parts, a measurement with a 70 ns time window and 4096 bins of ~17ps width, and a 600ns time window with 4096 bins of ~146ps. The data was analyzed using standard available software.

III. RESULTS AND DISCUSSION

The physical characterization of our ZTO nanowires was initiated by measuring the XRD patterns. As shown in figure 1 c), the XRD peaks are very narrow indicating good quality crystal and the peak

positions are all well matched with the inverse spinel structure of ZTO (Reference card JCPDS 00-024-1470)[7]. The XRD does not show any additional peaks which would correspond to extra phases from ZnO or SnO_2, indicating the etching process properly removed such phases.

The diffuse reflectance spectra was measured to obtain the absorption spectra[7]. This method is well suited to the ZTO nanowires because they are opaque due to significant light scattering which makes a direct absorption measurement difficult. The diffuse reflectance is then converted into absorbance with the Kubleka-Munk function given by[19]

$$F_{KM}\big(R(h\upsilon)\big) = \frac{(1-R(h\upsilon))^2}{2\,R(h\upsilon)} = \frac{\alpha(h\upsilon)}{S} \qquad (1)$$

Here, $R(h\upsilon)$ is diffuse reflectance, $\alpha(h\upsilon)$ is absorption coefficient, and S is a constant scattering coefficient. The absorption coefficient near the absorption edge can be related to photon energy ($h\upsilon$) by[20]

$$\alpha(h\upsilon) = A\,\frac{(h\upsilon - E_g)^n}{h\upsilon} \qquad (2)$$

Here, A is a proportionality constant for the transition, E_g is the band gap of the material, and $h\upsilon$ is the photon energy. By combining equations (1) and (2) we can fit the F_{KM} edge for different values of n. The measured F_{KM} and its' best fit with n=1.5 is shown in figure 2. A n=1.5 is consistent with a direct forbidden transition mechanism. From this fit we also obtain an estimate of the band gap energy of 3.75 eV (330 nm) which is consistent with the band gap of 3.71eV reported by Aviles et al[9], who also concluded a direct forbidden transition. The direct forbidden nature of the band edge transition in ZTO is also supported by first principle calculations of Segev et al[21]. For comparison to the absorption data, the broad band PLE spectrum is also shown in figure 2. This PLE data was taken at the observed PL peak of 1.87eV, which will be discussed in detail later, and shows a clear peak near the band edge at around 3.97 eV(312 nm)[22]. The PLE indicates emissions are excited at or above the band edge but are not excited by below band gap energy absorption which indicates no appreciable absorption states lie within the band gap. The PLE follows the trend of absorption near and below the band gap but drops off at higher excitation

energies, similar to what has been reported in the literature for other materials[22–24]. The data indicates that at higher excitation energies, additional recombination channels become available and thus the carriers does not relax through the observation energy of our PLE[25–27].

Being a direct forbidden material, the band to band recombination will be almost zero and the vast majority of the excited carrier recombination will be through mid-band gap states. To study these intrinsic defect states we start by looking at the room temperature (RT) steady state PL spectra. Due to the very broad nature of the PL observed, we first translate the measured data versus wavelength to energy, following the procedure outlined by Pelant and Valenta [26]. This removes the distortion caused by the changing spectral bandwidth (in energy) of the measurement system, and the resulting PL data versus energy is shown in figure 3. This plot shows the lack of any PL emission near 3.647 eV (340 nm), indicating that the observed PL is not related to band edge states or shallow donor/acceptor states. Thus the PL measurements further support the direct forbidden transition conclusion from the diffuse reflectance measurements. The PL plot does show two very broad visible emission peaks at high pump intensity (10 mJ/cm^2), a red peak centered at 1.86eV and a blue peak at 2.81eV. Note that the blue emission peak is very weak at lower pump intensity (50 μJ/cm^2) as shown in inset of figure 3, we will return to this issue later. Also shown in the figure is a fit of the measured spectrum to two Gaussian peaks, the quality of this fit indicates that both peaks are well represented by a Gaussian distribution function. In addition, both PL peaks have a very large Stokes' shift from the observed PLE/Absorption. A spectrally broad Gaussian peak with a large Stokes shift is consistent with deep level defect recombination in the strong electron phonon coupling[26] regime and similar characteristics have been reported in other materials such as ZnO[28], ZnS[29], and GaN[30].

We further analyzed the characteristics of the PL spectra by repeating the PL measurements at low temperature (LT). This is shown in figure 4 where the red emission peak blue shifted slightly (0.044 eV)

with increasing temperature, this is opposite to what would be expected for a band edge related transition[31]. The blue emission peak intensity, normalized at the blue peak position, is shown in the inset of figure 4. As seen from this figure any blue emission peak shift present is small and difficult to quantify due to the broad nature of the peaks, and the overlap with the stronger red emission peak. Regardless it is clear that if there is a shift, it is small. Also observed in this data is that the FWHM of the red and blue emission peaks decrease slightly at LT. To try and quantify these changes we preformed Gaussian fitting of the peaks and the FWHM of the red peak decreases from 0.654 eV to 0.591 eV at LT. However, the blue peak is relatively weak, particularly at LT, and overlaps with the stronger red peak thus the uncertainty in the FWHM fitting parameter of the blue peak is larger than any changes present and thus these changes cannot be quantified by fitting. Regardless, as the peaks remain quite broad and Gaussian, even at LT, we conclude that the transitions do not involve free carriers in band states but are inter-defect or intra-defect related transitions.

Additional information about the states involved in these transitions can be obtained from measurements of the PL intensity as a function of excitation power intensity. These measurements can modify the occupancies of the various defect states and thus the emission from them, potentially even saturating some defect levels. Figure 5 shows the LT and RT (inset) PL integrated intensities of both the red and blue peaks as a function of excitation intensity using a 310 nm pump. No shift of the red or blue emission peak positions with increasing intensity was observed at RT and LT; this type of behavior has also been observed in defect recombination center emission in ZnO[32,33] and $AgInS_2$[34]. The two PL peak intensities show similar pump intensity dependence at both RT and LT. At both RT and LT the blue emission intensity increases nearly linearly with excitation while the intensity of red emission saturates at higher excitation intensities. The saturation of the emission of defect states depends upon the defect

concentration and the lifetime of the states[35, 36]. In these nanowires the red states become saturated at higher excitation which results in increased PL intensity from the blue emission.

We also looked at the charge carrier dynamics of these transitions by measuring the Time Resolved PL (TRPL) at wavelengths across the entire emission spectrum (20 nm spacing) using 310 nm excitation at low intensity (0.18 mJ/cm^2). A representative subset of the data is shown in figure 6 where the top panel (a) in figure 6 is an expanded view of the first 10ns after excitation while the bottom panel (b) shows the full time window measured. The temporal decay was not seen to follow a single exponential decay function at any wavelength. The decay is more complex than can be fit with any physically meaningful number of exponential decays. Complex decays have been previously reported in ZnO[37–39] and ZnO:MgO[40] related defect recombination. Generally it is assumed that the complex nature of the decay is related to the random nature of the spacing between the defects associated with the transition[26]. Thus defects which are physically close in space have a faster decay rate while those with larger spacing decay slower. The overall measured decay thus contains contributions from the entire distribution and as such is very complex[26].

While the complex nature of the decay prevents us from extracting specific time constants for the transitions we can still obtain useful information from this data. First, the presence of the complex decay is itself an evidence of a defect to defect transition. Additionally, it is clear from these plots that the overall time decay of the PL is faster at shorter wavelengths and slower at longer wavelengths. Some of this is the much faster decay of the blue states transition compared to the red which will be explained shortly, however this trend continues even at longer wavelengths where there is little or no contribution from the blue defect states. This type of trend is also a characteristic feature of defect to defect recombination as defect sites which are closer together not only decay faster but also have a higher overall transition energy due to a larger coulomb interaction[20,26].

An alternative method to visualize what this wavelength dependent TRPL data means is to use the PL and TRPL information to calculate and plot the Time Resolved Emission Spectrum (TRES)[40,41]. This was done for our ZTO data and the resulting TRES plots are shown in figure 7. The most obvious observation from this view of the data is that the blue emission peak initially dominates the spectrum but disappears very rapidly, within a few hundred picoseconds. Once the blue peak vanishes the red peak becomes the dominant feature and decays very slowly, on the time scale of hundreds of nanoseconds. Thus there is a dramatic difference, 3 orders of magnitude, between the decay properties of the states responsible for the blue emission and those of the red emission.

To investigate the decay properties in more detail we also measured the TRPL as a function of excitation intensity. This was done to look for any changes in the decay characteristics and to see if at lower excitation intensities the decay might become less complex or maybe even single exponential. These curves are shown in Figure 8, but also in a different format, where we are looking at the decay as a function of time for the wavelengths corresponding to the blue peak (a) and red peak (b). As seen in the plots the decays do not change their overall characteristics and remain very complex even at the lowest excitations used. Also as observed in the previous wavelength dependent TRPL and TRES plots, the blue emission decays very fast and the red emission decays much more slowly. However, both peaks show an initial faster decay which transitions to a much slower decay process at longer times. Thus the primary difference is that the blue peak has a much larger portion of the decay being due to the faster process and as such the slow decay is down several orders of magnitude compared to the red peak decay. Both peaks show a common feature in which the decay speeds up considerably as the excitation intensity is initially increased, but that this increasing decay speed saturates at the high excitations intensities. This increase in the decay speed is consistent with what is expected for defect to defect recombination as at higher intensities there is a higher probability of excited defect states being closer to each other, and thus an

increase in the amount of fast decay. Our observations are consistent with previous reports on defect recombination in ZnO[32] and is opposite to what is observed in exciton emission decays[32].

Still unexplained however is the reason for the much faster overall decay of the blue peak compared to the red. Thus to understand this and to further develop our picture of the band structure and carrier dynamics in the ZTO nanowires we also looked at the rise time characteristics at wavelengths close to the observed red and blue PL peaks, these are shown in figure 9. There is a small but discernible delay of approximately 17 ps in the rising edge of the 454 nm signal with respect to the instrument response function (IRF). This delay is too long[27] to be intra-band scattering of the excited carriers and thus is likely due to carrier capture into the defect states associated with the blue transition. We also see a much longer delay of about 68 ps for the rising edge of the 674 nm wavelength signal compared to the IRF signal. This rise time behavior is counter to what Han et al[16] observed in ZnO where they see no delay in PL rise time. The slower rise of the red could indicate a slower carrier capture process for the red defect states compared to the blue, but the rise of the red emission also coincides with the fast decay of the blue emission. Thus it is also possible that the red defect states are fed from the blue states and not directly from the band edge. This seems the more likely scenario as it would explain not only the very fast decay of the blue peak but also the associated weak emission from it. Thus we conclude that much of the fast decay of the blue peak is due to non-radiative charge transfer from the blue defect states to the red states which limits the total emission from the blue states. In addition, since the decay from the red states is relatively slow these states saturate at high excitation intensity which results in more emission from the blue states at these higher excitations.

While these measurements characterize the behavior of the emissive states in the ZTO nanowires and give us some indication of where they are in the band structure of the ZTO, they do not allow us to directly associate these states with particular defects. However, it should be noted that emission similar

to our observed red emission peak has been reported by numerous groups [18,42–44]. While several possible explanations have been suggested, such as Zn or Sn vacancies, lack of Zn/Sn stoichiometry, or Oxygen vacancies, the origin of this emission is still unclear. Reports on the structural characterization of inverse spinel structure ZTO thin films show a lack of good atomic ordering compared to inverse spinel structure Cd_2SnO_4 (Cadminum Stannate) thin film[45]. This disorder in ZTO is due to the Zn^{2+} and Sn^{4+} cations that randomly occupy the octahedral sites and result in a deviation in the Zn:Sn stoichiometry. A recent report observed a measurable shift in the peak position of the red peak with changes in Zn/Sn stoichiometry, indicating that stoichiometry plays a role in the red emission. A blue or blue-green emission peak has also been observed by other groups [46–50] and is generally associated with states that are created by oxygen vacancies present in the ZTO. The exact type and number of defect states is likely to be somewhat dependent on the method and parameters used in the synthesis of the ZTO nanowires and likely the reason for the variation in the experimental results and explanations.

Since the peak position of our blue peak is slightly different than what has been previously reported[46–50], we also investigated the origin of our blue emission by studying the effect of annealing on our ZTO nanowires. The as-grown, annealed in air, and annealed in vacuum samples were studied using XRD, Raman Spectrum, and RT PL. The XRD of the three samples are shown in figure 10 a) and do not indicate any noticeable change in XRD peak position or width, suggesting no significant changes in crystal quality with annealing. We also measured the Raman spectrum for the three samples at RT, which are shown in figure 10 b). The Raman modes (670 cm^{-1}(A_{1g}), 528 cm^{-1}(F_{2g}), 437 cm^{-1}(E_g), 378 cm^{-1}(F_{2g}) & 227 cm^{-1}(F_{2g}) belong to ZTO and are consistent with previous results[51–53]. By annealing in air and vacuum the Raman shows a slight improvement in the crystallinity of the ZTO sample as indicated by a small increase of the 437 cm^{-1} peak, as shown in the inset. Regardless the changes are quite subtle. To investigate whether or not the blue peak is related to oxygen vacancies we measured the RT PL of as-grown, annealed

in air, and vacuum annealed ZTO NWs samples, which is shown in Figure 11. From this figure it is clear that the relative intensity of the blue emission peak increases compared to the red peak for the vacuum annealed samples. There are two possible explanations for this, first the vacuum annealing process may decrease the surface absorbed oxygen and thus increase the oxygen vacancies in the sample. Second, it is also possible that hydrogen atoms passivate some of the oxygen vacancies in the sample[54] and under vacuum annealing some of these hydrogen atoms are removed thus increasing the active oxygen vacancies. Either mechanism yields more active oxygen vacancies after vacuum annealing, and thus more blue emission. As a control, the PL of the air annealed sample was also measured and did not show any change in the relative blue emission intensity. This confirms that the increase in the blue peak with vacuum annealing is not the result of changes to the crystalline quality from annealing but is a result of changes in the number of oxygen vacancies.

A final proposed energy band diagram is shown in figure 12, complete with carrier relaxation paths. While it is possible to determine the relative positions of the defect states from our measurements, it is not possible to determine the absolute positions of these states relative to the conduction and valence bands. Our data indicates that none of the optically observed transitions are associated with band edge states, thus all of our transitions must involve electron and hole defect/trap states. In addition, due to the n-type behavior of ZTO nanowires[14,44], the electron trap states will be mostly filled with electrons, even in equilibrium, and as such the transition from the CB to the electron traps states does not show up in our measurements. Since our measurements do show a slight delay in the blue emission, it follows that this must be due to hole capture into the shallower hole trap state associated with the blue transition, as shown in the figure. The fast decay of the blue emission coupled with the very low intensity of the blue emission indicates that the blue decay must be mostly carrier transfer to the red hole defect states, also illustrated

in figure 14. The observed slow decay of the red states is thus consistent with the increased blue emission at higher excitations as the red states fill with holes.

IV. CONCLUSIONS

We have studied the optical properties of ZTO nanowires prepared by chemical vapor deposition using diffuse reflectance spectroscopy, PL, and Time Resolved Emission Spectroscopy. From the diffuse reflectance and PL measurements, we conclude that our ZTO nanowires have a direct forbidden transition. The absence of a direct band to band recombination path will increase the carrier lifetime and thus provide improved carrier transport when used for this function in DSSC and QDSSC applications. We observe two broad emission peaks in the emission spectra, a red peak at 1.86eV with a slow decay, and a weaker but much faster decaying blue peak at 2.81eV. Both peaks are the result of defect to defect transitions and we show that the blue emission states are related to oxygen vacancies while the red transition is likely due to a lack of Zn/Sn stoichiometry. In addition, we show that the red states are populated through the blue states which limits the emission from the blue states. Based on our experimental results we propose an energy band diagram for ZTO nanowires.

Acknowledgement:

The authors would like to thank Dr. Bruce Parkinson for the generous use of his UV-VIS spectrophotometer for the diffuse reflectance measurements, and Dr. Marc Achermann of the Lucerne University in Switzerland for fruitful discussion and suggestions on this manuscript. Also, we would like to thank Dr. William Rice, University of Wyoming and Dr. TeYu Chen, University of Wyoming for helpful suggestions on the experiments and discussion on the manuscript. This work was supported by the U.S. Department of Energy, Office of Basic Energy Sciences, Division of Materials Sciences and Engineering under Award DE-FG02-10ER46728.

Reference:

[1] B. O'Regan and M. Gratzel, Nature **353**, 737 (1991).
[2] B. Tan, E. Toman, Y. Li, and Y. Wu, J. Am. Chem. Soc. **129**, 4162 (2007).
[3] P. V. Kamat, Acc. Chem. Res. **45**, 1906 (2012).
[4] A. Kongkanand, K. Tvrdy, K. Takechi, M. Kuno, and P. V. Kamat, J. Am. Chem. Soc. **130**, 4007 (2008).
[5] M. Law, L.E. Greene, J.C. Johnson, R. Saykally, and P. Yang, Nat. Mater. **4**, 455 (2005).
[6] M. Grätzel, Inorg. Chem. **44**, 6841 (2005).
[7] J. Chen, L. Lu, and W. Wang, J. Phys. Chem. C **116**, 10841 (2012).
[8] T. Lana-Villarreal, G. Boschloo, and A. Hagfeldt, J. Phys. Chem. C **111**, 5549 (2007).
[9] M.A. Alpuche-Aviles and Y. Wu, J. Am. Chem. Soc. **131**, 3216 (2009).
[10] Q. Dai, J. Chen, L. Lu, J. Tang, and W. Wang, Nano Lett. **12**, 4187 (2012).
[11] H.Q. Chiang, J.F. Wager, R.L. Hoffman, J. Jeong, and D.A. Keszler, Appl. Phys. Lett. **86**, 13503 (2005).
[12] T. Minami, S. Takata, H. Sato, and H. Sonohara, J. Vac. Sci. Technol. A **13**, 1095 (1995).
[13] M. Miyauchi, Z. Liu, Z.-G. Zhao, S. Anandan, and K. Hara, Chem. Commun. **46**, 1529 (2010).
[14] W.B. Jackson, R.L. Hoffman, and G.S. Herman, Appl. Phys. Lett. **87**, 193503 (2005).
[15] D. Chen, J. Xu, B. Liang, X. Wang, P.-C. Chen, C. Zhou, and G. Shen, J. Mater. Chem. **21**, 17236 (2011).
[16] N.S. Han, H.S. Shim, J.H. Seo, S.Y. Kim, S.M. Park, and J.K. Song, J. Appl. Phys. **107**, 1 (2010).
[17] and Y.Y. Jianxiong Wang, Xiao Wei Sun, Shishen Xie, Weiya Zhou, Cryst. Growth Des. **8**, 707 (2008).
[18] T. Lim, H. Kim, M. Meyyappan, and S. Ju, ACS Nano 4912 (2012).
[19] M. Nowak, B. Kauch, and P. Szperlich, Rev. Sci. Instrum. **80**, 46107 (2009).
[20] J.I. Pankove, *Optical Processes in Semiconductors* (Prentice-Hall, Englewood Cliffs, N.J, 1971).
[21] D. Segev and S.-H. Wei, Phys. Rev. B **71**, 125129 (2005).
[22] Z. Fu, H.K. Yang, B.K. Moon, B.C. Choi, and J.H. Jeong, Curr. Appl. Phys. **9**, 1360 (2009).
[23] a. D. Dinsmore, D.S. Hsu, S.B. Qadri, J.O. Cross, T. a. Kennedy, H.F. Gray, and B.R. Ratna, J. Appl. Phys. **88**, 4985 (2000).
[24] C. Jin, J. Yu, L. Sun, K. Dou, S. Hou, J. Zhao, Y. Chen, and S. Huang, J. Lumin. **66**–**67**, 315 (1995).
[25] L. Museur, E. Feldbach, and A. Kanaev, Phys. Rev. B - Condens. Matter Mater. Phys. **78**, 1 (2008).
[26] I. Pelant and J. Valenta, *Luminescence Spectroscopy of Semiconductors* (Oxford University Press, Oxford ; New York, 2012).
[27] R.P. Prasankumar and A.J. Taylor, *Optical Techniques for Solid-State Materials Characterization* (CRC Press, 2011).
[28] F. Leiter, H. Alves, D. Pfisterer, N.G. Romanov, D.M. Hofmann, and B.K. Meyer, Phys. B Condens. Matter **340**–**342**, 201 (2003).
[29] S. Shionoya, T. Koda, K. Era, and H. Fujiwara, J. Phys. Soc. Japan **19**, 1157 (1964).
[30] M. a. Reshchikov and H. Morkọ, J. Appl. Phys. **97**, 1 (2005).
[31] L.E. Greene, M. Law, J. Goldberger, F. Kim, J.C. Johnson, Y. Zhang, R.J. Saykally, and P. Yang, Angew. Chemie - Int. Ed. **42**, 3031 (2003).
[32] J.V. Foreman, Photoexcited Emission Efficiencies of Zinc Oxide by Photoexcited Emission Efficiencies of Zinc Oxide, 2009.
[33] M. Li, G. Xing, G. Xing, B. Wu, T. Wu, X. Zhang, and T.C. Sum, Phys. Rev. B - Condens. Matter Mater. Phys. **87**, 1 (2013).

[34] J. Krustok, J. Raudoja, M. Krunks, H. Mändar, and H. Collan, J. Appl. Phys. **88**, 205 (2000).
[35] M. Reshchikov and R. Korotkov, Phys. Rev. B **64**, 1 (2001).
[36] J.G.S. Jr, J. V. Foreman, J. Liu, and H.O. Everitt, Appl. Phys. Lett. **103**, 201110 (2013).
[37] B. Guo, Z.R. Qiu, and K.S. Wong, Appl. Phys. Lett. **82**, 2290 (2003).
[38] S. Lettieri, L. Santamaria Amato, P. Maddalena, E. Comini, C. Baratto, and S. Todros, Nanotechnology **20**, 175706 (2009).
[39] S. Lettieri, V. Capello, L. Santamaria, and P. Maddalena, Appl. Phys. Lett. **103**, (2013).
[40] S. Rakshit and S. Vasudevan, J. Phys. Chem. C **112**, 4531 (2008).
[41] A.S.R. Koti, M.M.G. Krishna, and N. Periasamy, J. Phys. Chem. A **105**, 1767 (2001).
[42] Q.R. Hu, P. Jiang, H. Xu, Y. Zhang, S.L. Wang, X. Jia, and W.H. Tang, J. Alloys Compd. **484**, 25 (2009).
[43] K.J. Chen, F.Y. Hung, Y.T. Chen, S.J. Chang, and Z.S. Hu, Mater. Trans. **51**, 1340 (2010).
[44] M. Lei, Y. Sheng, L. Wan, K. Bi, K. Huang, R. Jia, J. Liu, and Y. Wang, J. Alloys Compd. **657**, 394 (2016).
[45] D.L. Young, D.L. Williamson, and T.J. Coutts, J. Appl. Phys. **91**, 1464 (2002).
[46] J.-W. Zhao, L.-R. Qin, and L.-D. Zhang, Solid State Commun. **141**, 663 (2007).
[47] J.X. Wang, S.S. Xie, Y. Gao, X.Q. Yan, D.F. Liu, H.J. Yuan, Z.P. Zhou, L. Song, L.F. Liu, W.Y. Zhou, and G. Wang, J. Cryst. Growth **267**, 177 (2004).
[48] J. Wang, X.W. Sun, S. Xie, W. Zhou, and Y. Yang, Cryst. Growth Des. **8**, 707 (2008).
[49] F.-L.K. and D.H.L.N. Ming Lei, J. Nanosci. Technol. **10**, 8432 (2010).
[50] M. Lei, F.-L. Kwong, and D.H.L. Ng, J. Nanosci. Nanotechnol. **10**, 8432 (2010).
[51] V.G.S. and O.V.S. N.V. Porotnikov, 932 (1983).
[52] M. V Nikolić, T. Ivetić, D.L. Young, K.M. Paraskevopoulos, T.T. Zorba, V. Blagojević, P.M. Nikolić, D. Vasiljević-Radović, and M.M. Ristić, Mater. Sci. Eng. B **138**, 7 (2007).
[53] V. Sepelak, S.M. Becker, I. Bergmann, S. Indris, M. Scheuermann, A. Feldhoff, C. Kubel, M. Bruns, N. Sturzl, A.S. Ulrich, M. Ghafari, H. Hahn, C.P. Grey, K.D. Becker, and P. Heitjans, J. Mater. Chem. **22**, 3117 (2012).
[54] J. Anderson and G.V. de W. Chris, Reports Prog. Phys. **72**, 126501 (2009).

Figure captions:

Figure 1- Typical SEM image of our ZTO nanowires network (a) SEM image of nanowire (b) XRD data of ZTO nanowires(c)

Figure 2- Calculated absorbance from measured diffuse reflectance spectra for ZTO nanowire (red), the absorption spectra of direct forbidden transitions (green) fit and PLE measured at 640 nm (blue).

Figure 3- PL of ZTO nanowires excited by 310 nm laser (black), a fit of the main defect peak to two peak gaussian function (green), red peak fit (red) and blue peak fit (blue), Inset shows PL at low excitation intensity

Figure 4- Low temperature (LT) and Room temperature (RT) PL, inset: expanded view of blue peak normalized at blue peak emission

Figure 5- Excitation intensity dependent PL at RT (a) and LT (b)

Figure 6- PL decay of ZTO nanowires (a) for times up to 10 ns to illustrate the fast decay components and (b) for times up to 550 ns showing the slower decay trends.

Figure 7- Time Resolved Emission Spectrum (TRES) of ZTO nanowires.

Figure 8- Intensity dependent TRPL decay of blue (a) and red (b) emission peaks

Figure 9- Instrument response function (black) and the time resolved PL curves at 454 nm (blue) and 674 nm (red) showing the differences in the rise time of the signals.

Figure 10- (a) XRD of as-grown (blue), vacuum annealed (green) and air annealed (red) ZTO nanowires, and (b) Raman of as-grown (blue), vacuum annealed (green) and air annealed (red) ZTO nanowires (inset: shows the 437 cm^{-1} peak)

Figure 11- PL of as-grown (blue), vacuum annealed (green) and air annealed (red) ZTO nanowires Figure 12- Proposed energy band diagram for the ZTO nanowires showing the defect states and the transitions between the states

Figure 1 a), b) & c)

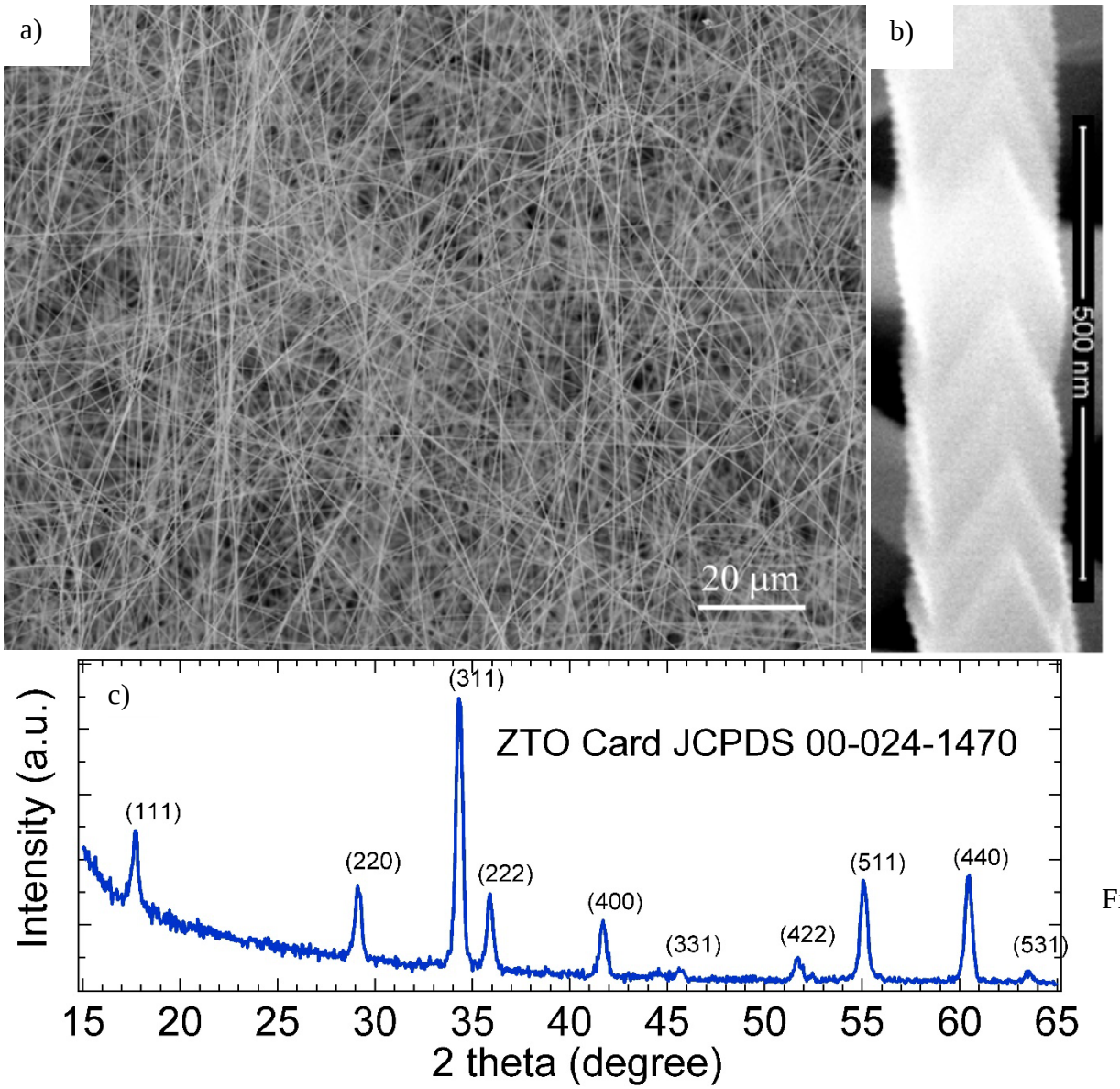

Figure 2

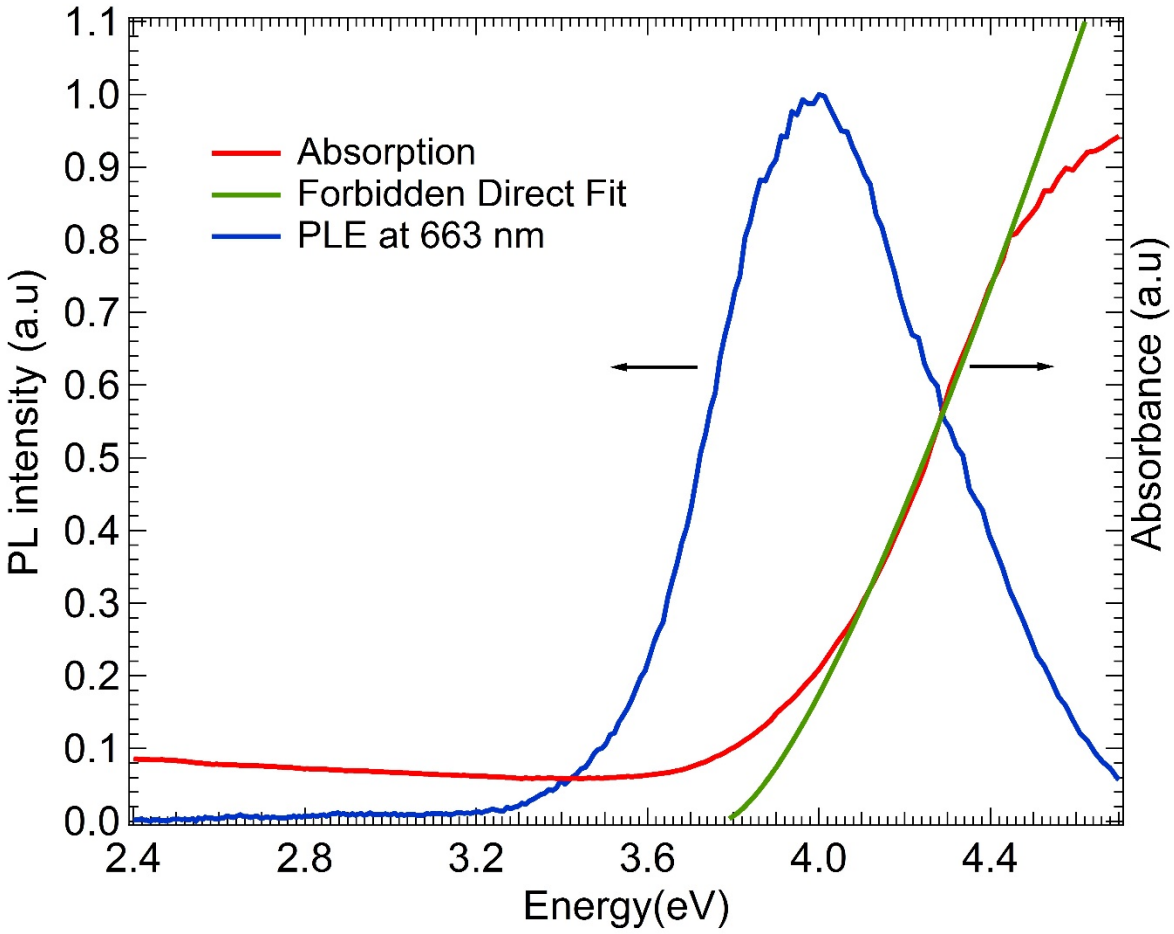
Absorption
Forbidden Direct Fit
PLE at 663 nm
PL intensity (a.u)
Absorbance (a.u)
Energy(eV)
0.0
0.1
0.2
0.3
0.4
0.5
0.6
0.7
0.8
0.9
1.0
1.1
2.4
2.8
3.2
3.6
4.0
4.4

Figure 3

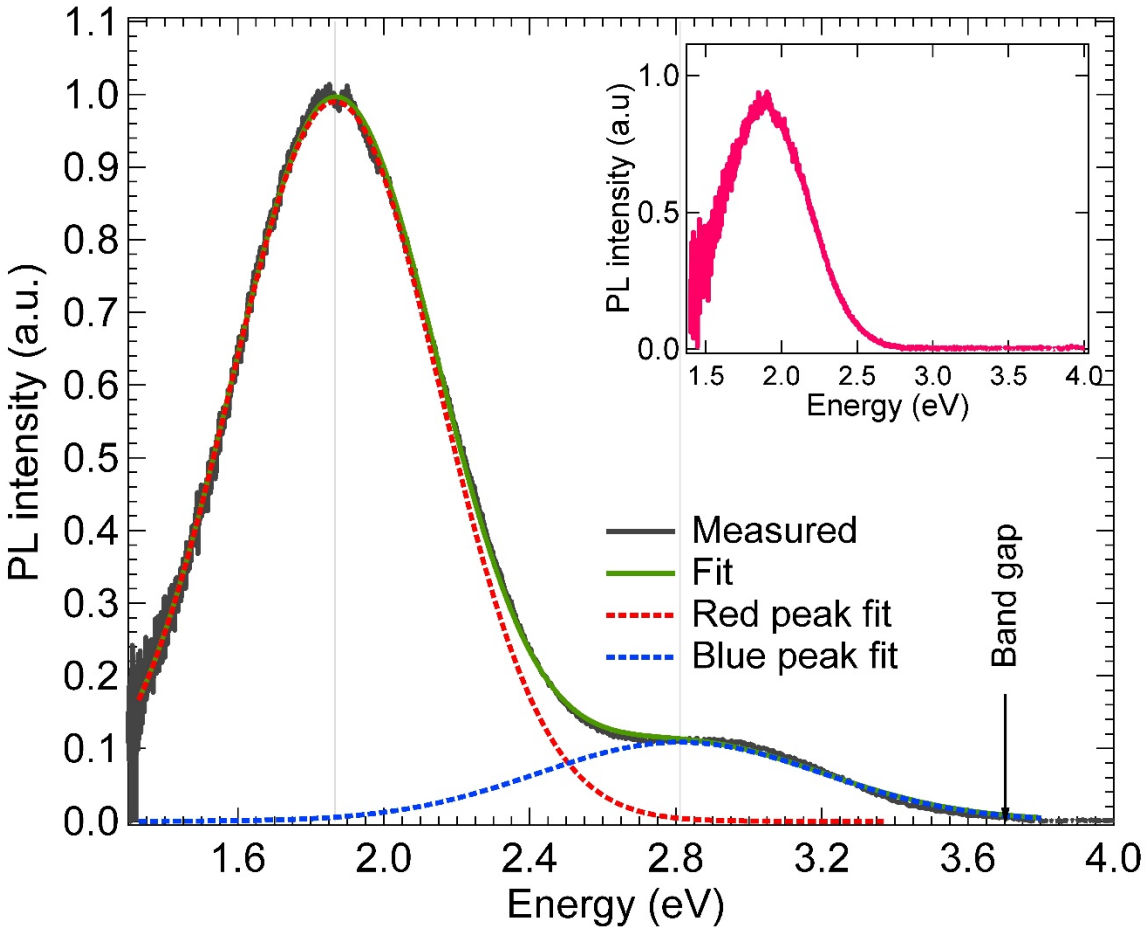
PL intensity (a.u.)
Energy (eV)
Measured
Fit
Red peak fit
Blue peak fit
Band gap
PL intensity (a.u)
Energy (eV)

Figure 4

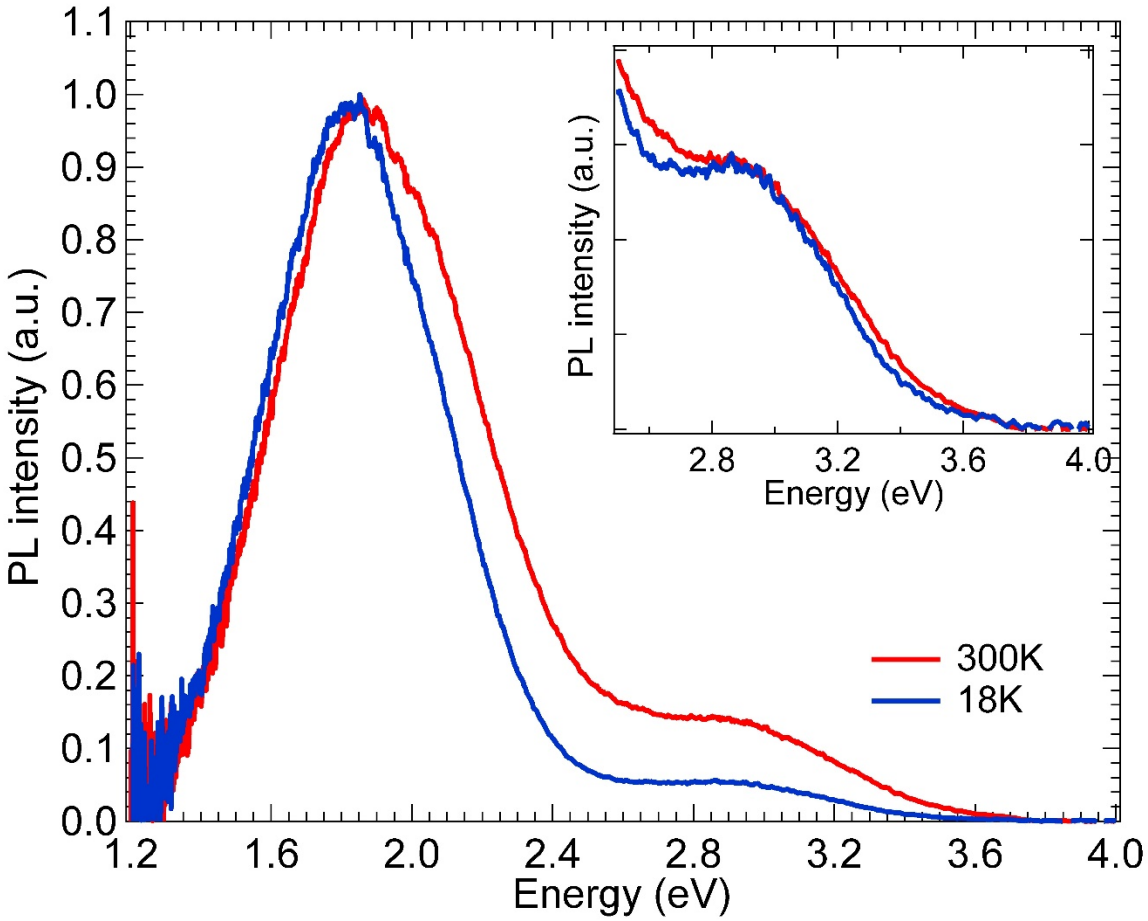

Figure 5

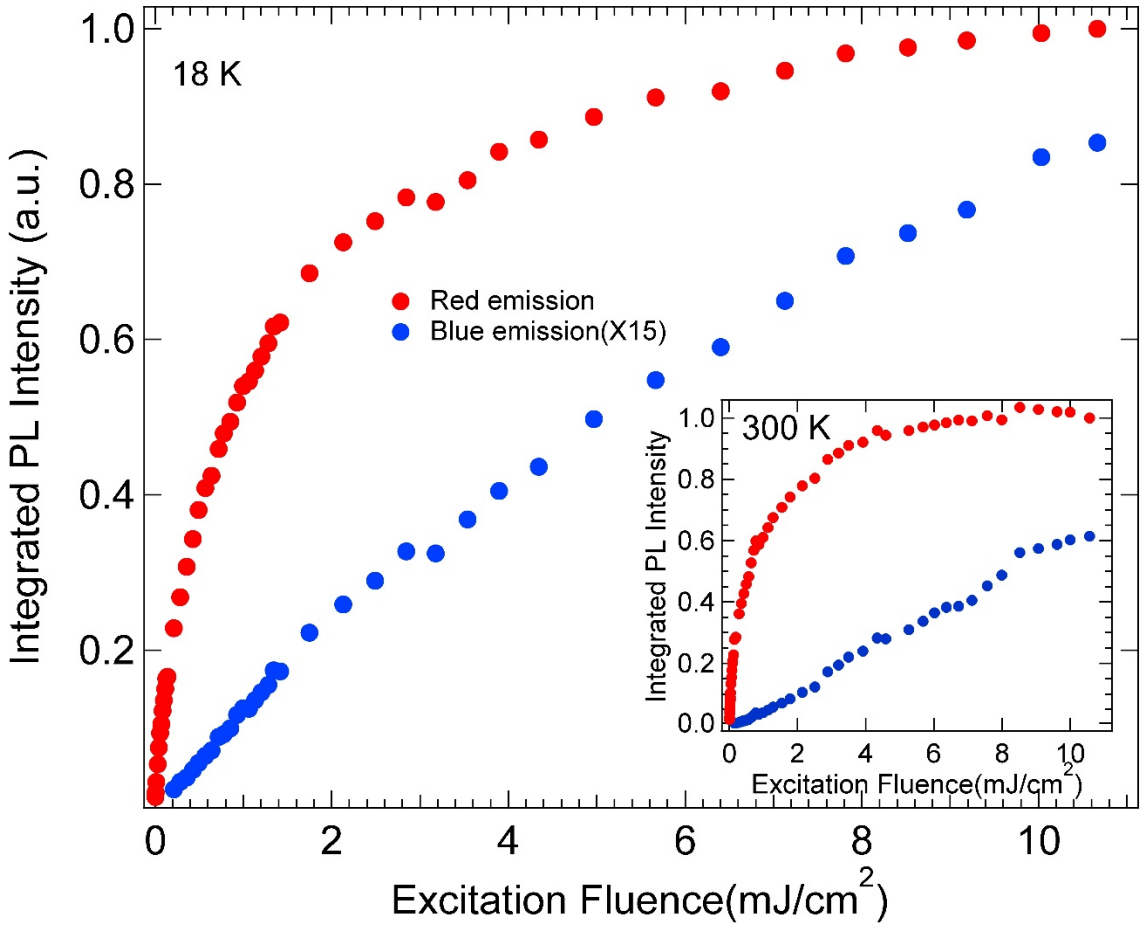
18 K
Red emission
Blue emission(X15)
Integrated PL Intensity (a.u.)
Excitation Fluence(mJ/cm2)
300 K
Integrated PL Intensity
Excitation Fluence(mJ/cm2)

Figure 6 a) & b)

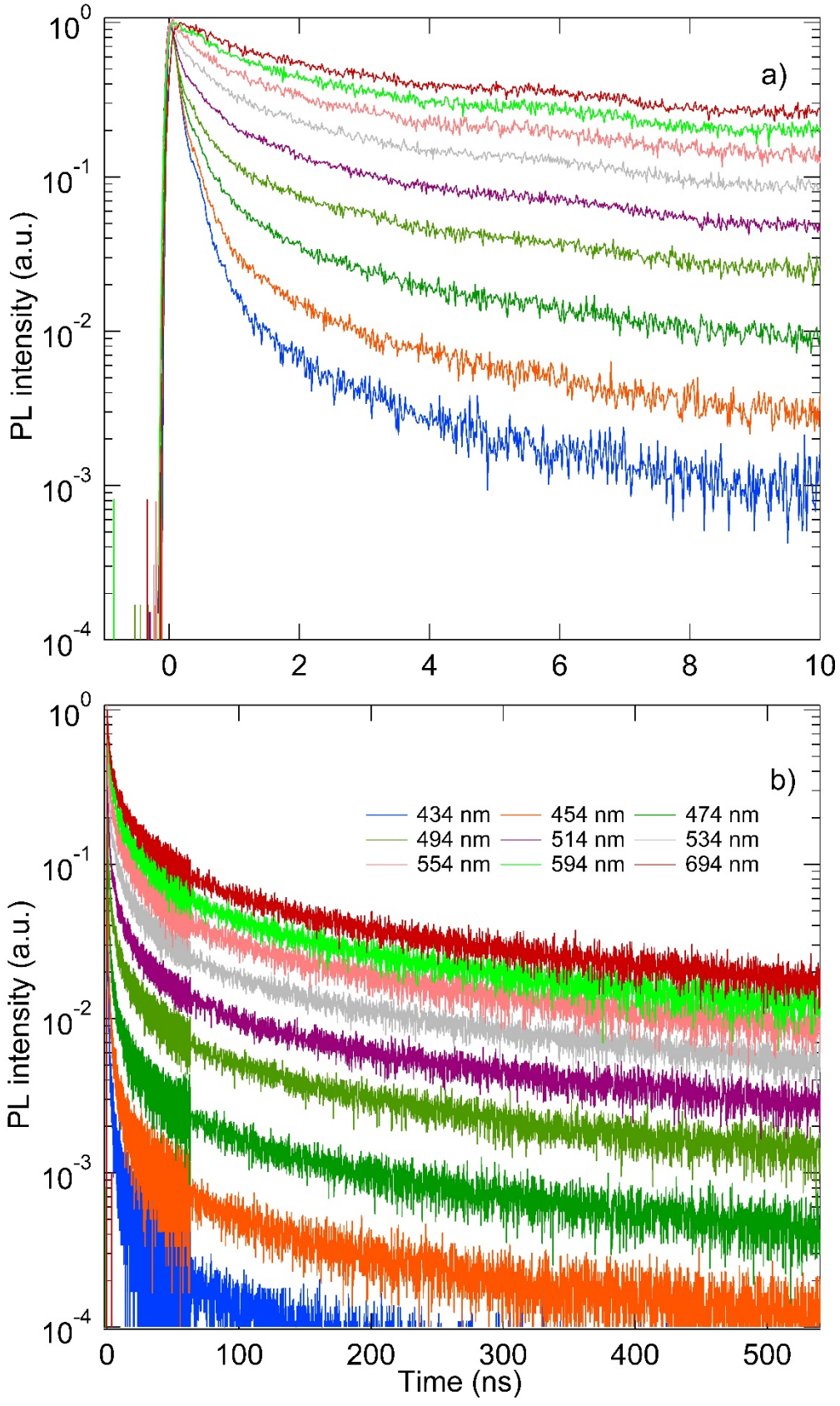
a)
b)
PL intensity (a.u.)
Time (ns)
434 nm
454 nm
474 nm
494 nm
514 nm
534 nm
554 nm
594 nm
694 nm

Figure 7

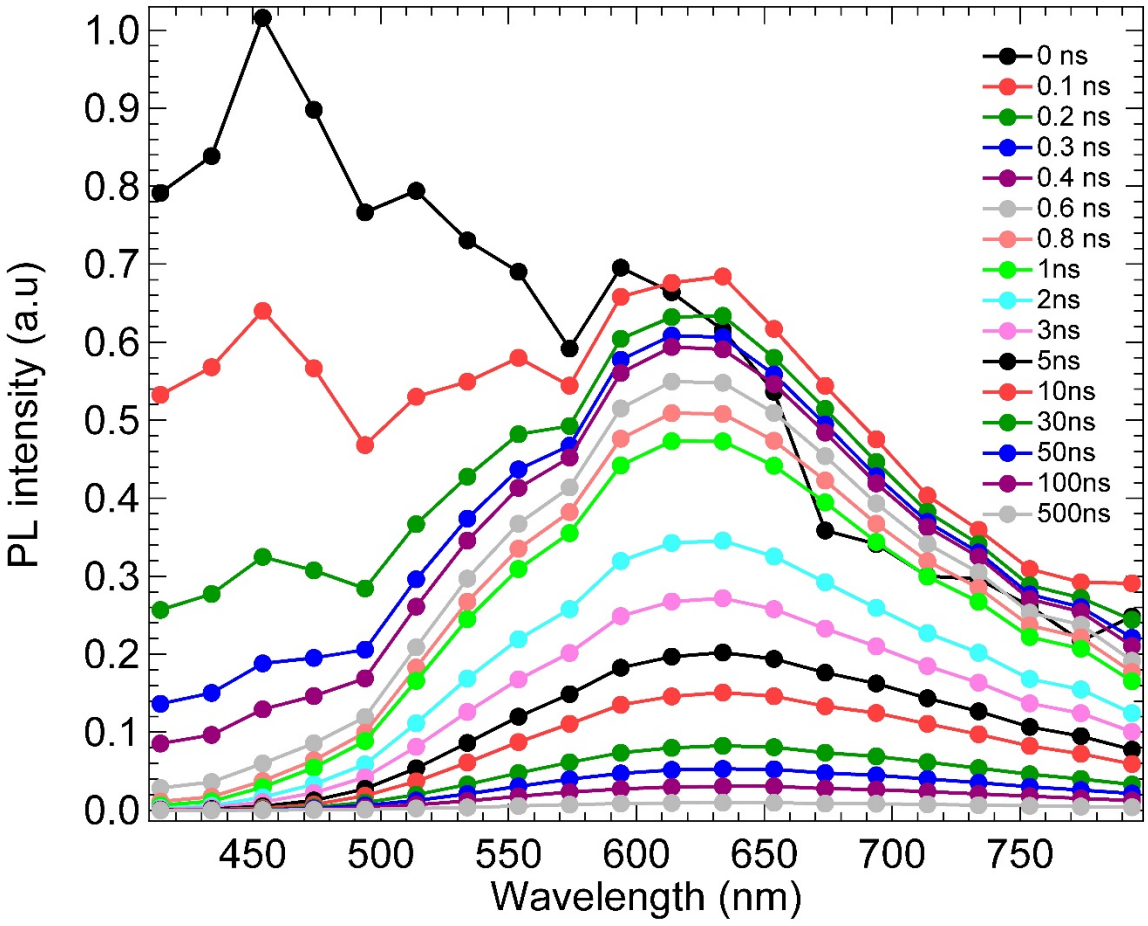
PL intensity (a.u)
Wavelength (nm)
0 ns
0.1 ns
0.2 ns
0.3 ns
0.4 ns
0.6 ns
0.8 ns
1ns
2ns
3ns
5ns
10ns
30ns
50ns
100ns
500ns

Figure 8 a) & b)

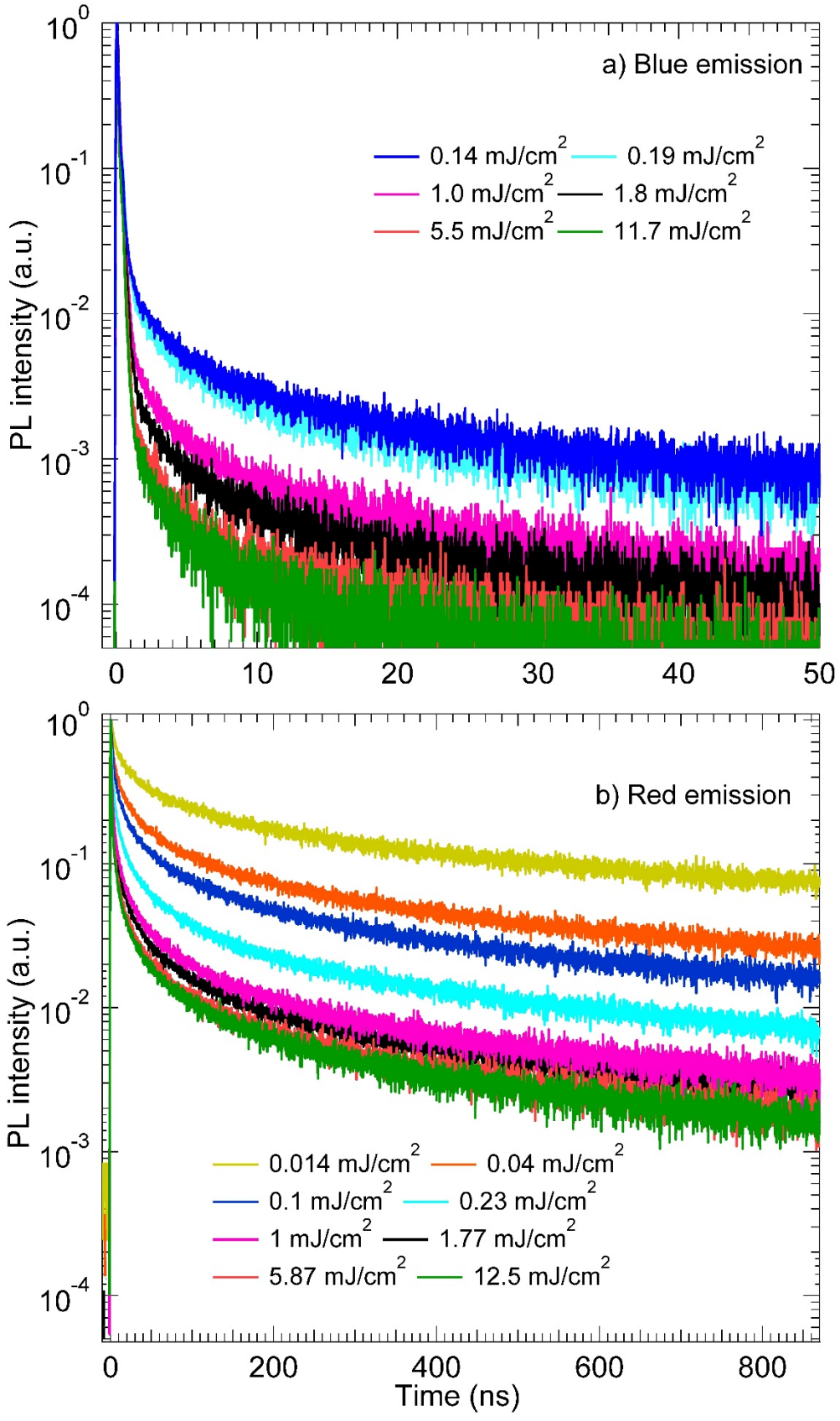
a) Blue emission
0.14 mJ/cm2
0.19 mJ/cm2
1.0 mJ/cm2
1.8 mJ/cm2
5.5 mJ/cm2
11.7 mJ/cm2
PL intensity (a.u.)
b) Red emission
0.014 mJ/cm2
0.04 mJ/cm2
0.1 mJ/cm2
0.23 mJ/cm2
1 mJ/cm2
1.77 mJ/cm2
5.87 mJ/cm2
12.5 mJ/cm2
Time (ns)

Figure 9

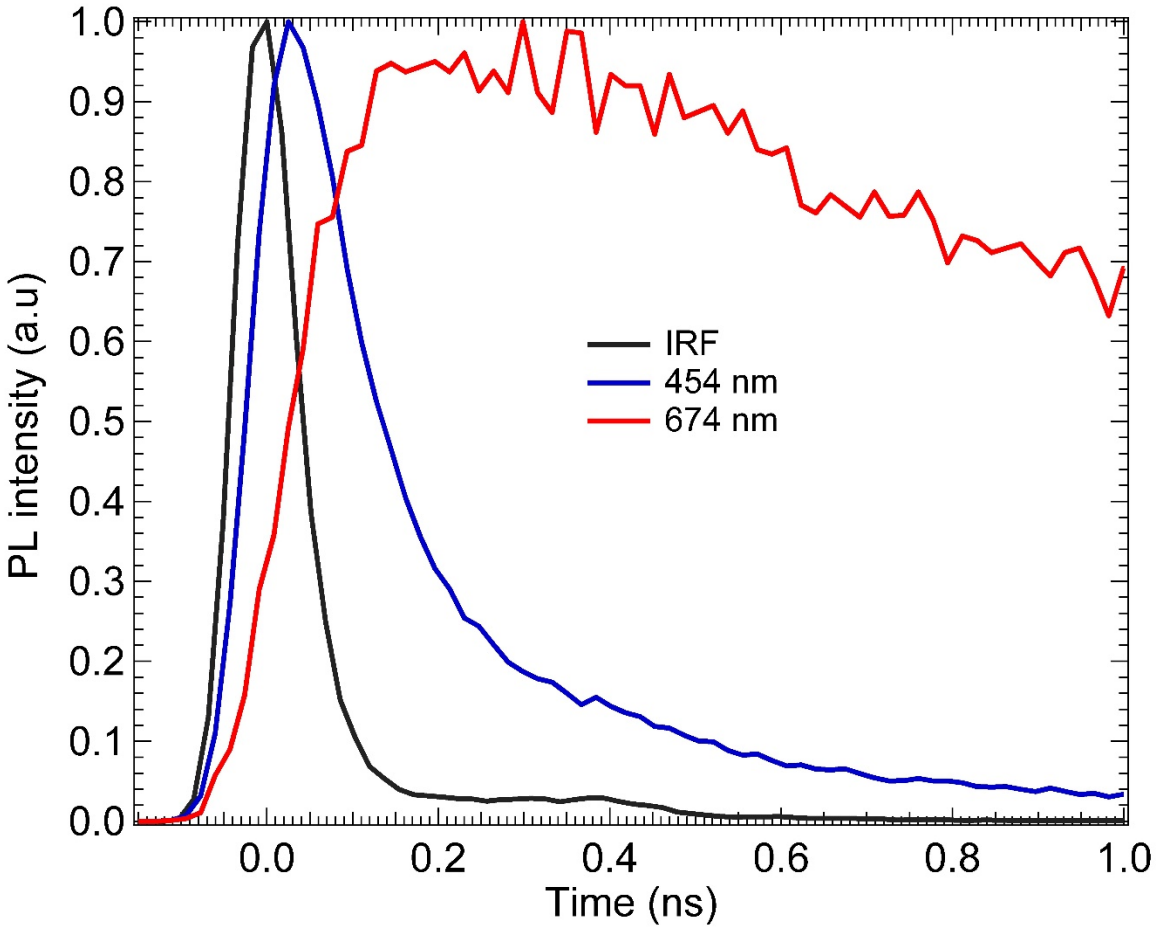
PL intensity (a.u)
Time (ns)
IRF
454 nm
674 nm
0.0
0.1
0.2
0.3
0.4
0.5
0.6
0.7
0.8
0.9
1.0
0.0
0.2
0.4
0.6
0.8
1.0

Figure 10 a) & b)

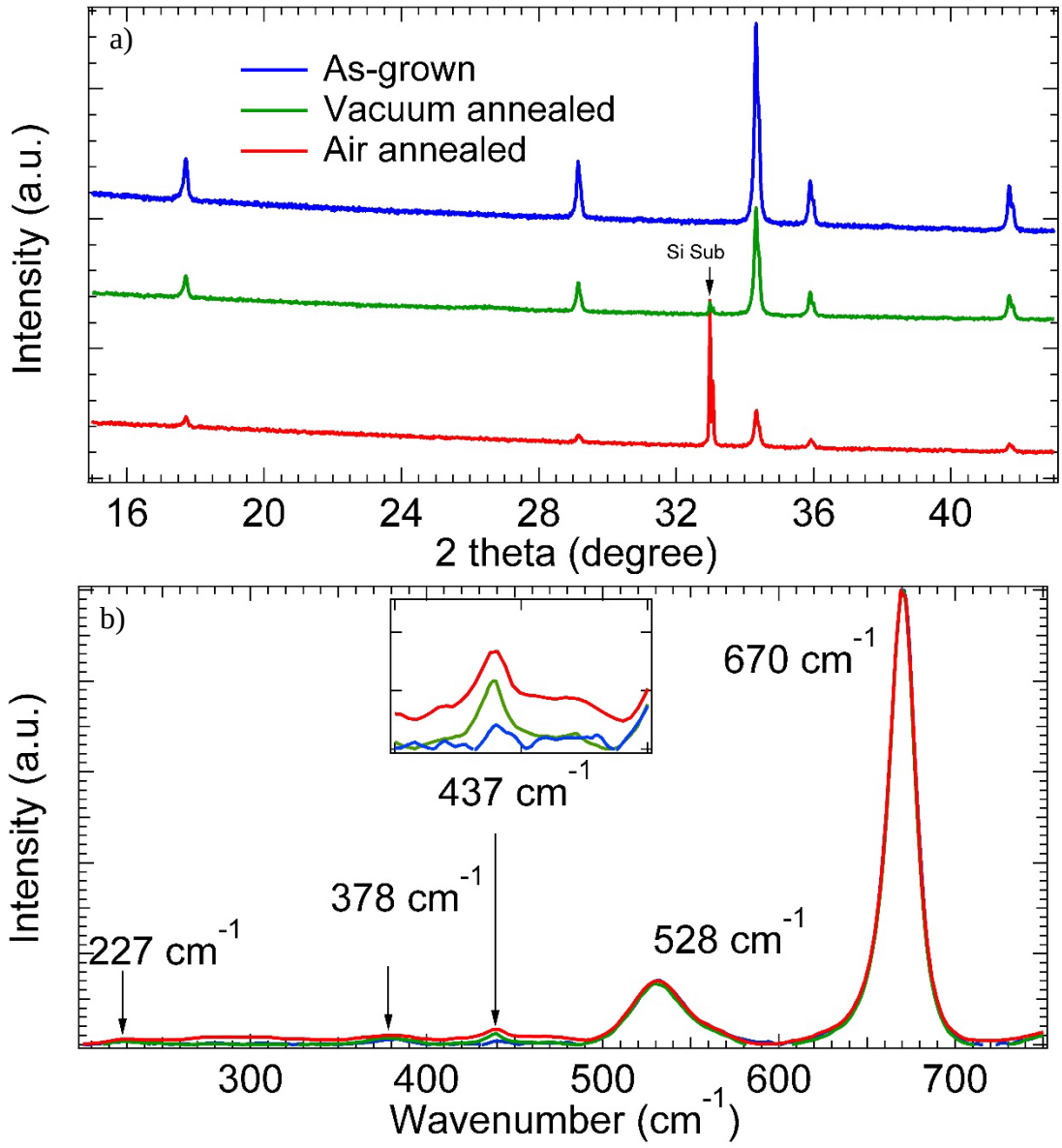
a)
As-grown
Vacuum annealed
Air annealed
Si Sub
Intensity (a.u.)
16
20
24
28
32
36
40
2 theta (degree)
b)
437 cm-1
670 cm-1
378 cm-1
227 cm-1
528 cm-1
Intensity (a.u.)
300
400
500
600
700
Wavenumber (cm-1)

Figure 11

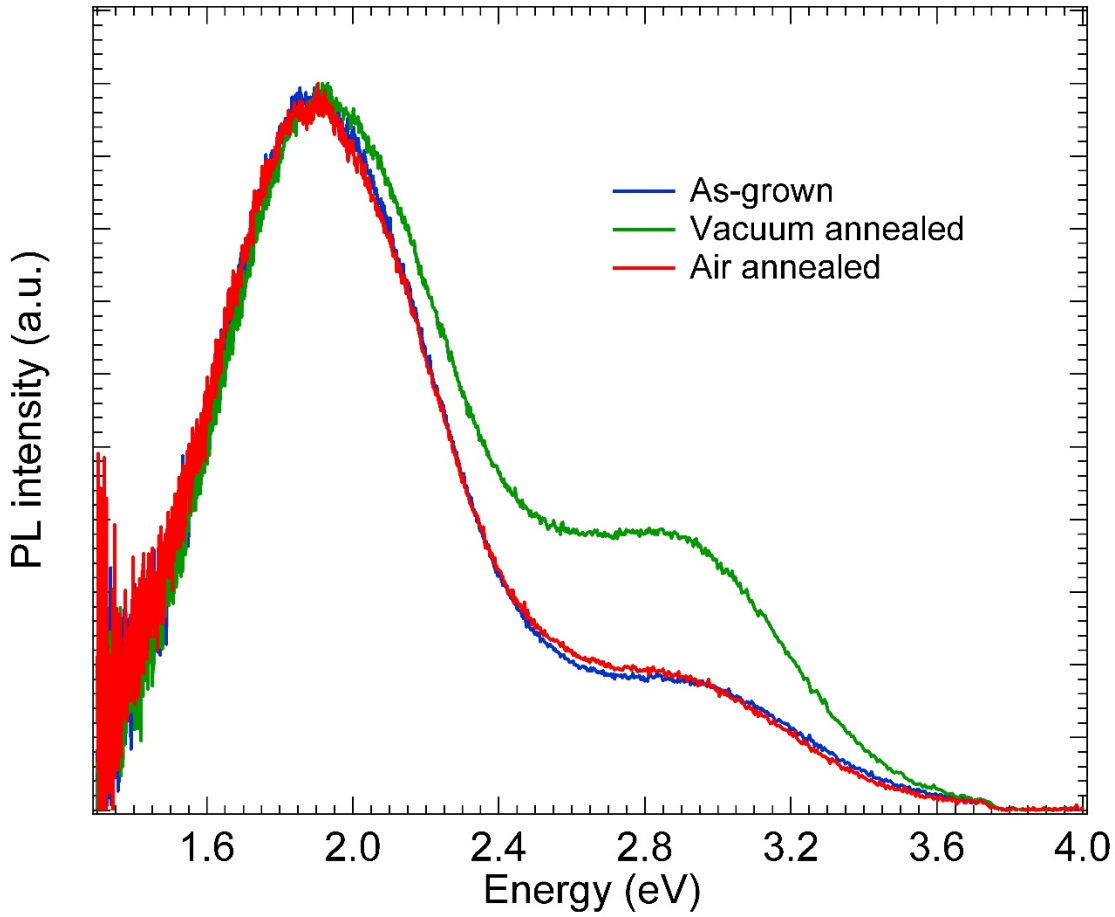
As-grown
Vacuum annealed
Air annealed
PL intensity (a.u.)
1.6
2.0
2.4
2.8
3.2
3.6
4.0
Energy (eV)

Figure 12